Tuning the electronic and magnetic properties of $NiBr_2$ via pressure

Soumen Bag,* Jesse Kapeghian, Onur Erten,† and Antia S. Botana‡
Department of Physics, Arizona State University, Tempe, Arizona 85287, USA

(Received 23 April 2024; revised 25 June 2024; accepted 8 August 2024; published 29 August 2024)

Transition metal dihalides (MX_2, M= transition metal, X= halide) have attracted much attention recently due to their intriguing low-dimensional magnetic properties. Particular focus has been placed in this family in the context of multiferroicity—a common occurrence in MX_2 compounds that adopt noncollinear magnetic structures. One example of helimagnetic multiferroic material in the dihalide family is represented by $NiBr_2$. Here, we study the evolution of the electronic structure and magnetic properties of this material under pressure using first-principles calculations combined with Monte Carlo simulations. Our results indicate there is significant magnetic frustration in $NiBr_2$ due to the competing interactions arising from its underlying triangular lattice. This magnetic frustration increases with pressure and is at the origin of the helimagnetic order. Further, pressure causes a sizable increase in the interlayer interactions. Our Monte Carlo simulations show that a large (threefold) increase in the helimagnetic transition temperature can be achieved at pressures of around 15 GPa. This indicates that hydrostatic pressure can indeed be used as a tuning knob to increase the magnetic transition temperature of $NiBr_2$.

DOI: 10.1103/PhysRevB.110.085161

I. INTRODUCTION

Two-dimensional (2D) van der Waals (vdW) magnets have been intensively studied as they provide powerful platforms to explore novel physical phenomena and to implement intriguing applications [1,2]. Transition metal dihalides represent an emerging class of 2D vdW magnets that can exhibit multiferroic order and noncollinear spin textures [3]. Within this family, the magnetic semiconductor NiI_2 has been the subject of much research in recent years [4–9]. In the bulk, two magnetic phase transitions take place in this material: one at 75 K to a collinear antiferromagnetic (AFM) state and one at 60 K to a helimagnetic state [10,11]. This noncollinear magnetic state simultaneously hosts a spin-induced ferroelectric polarization tunable with magnetic field, making NiI_2 a type-II multiferroic [12]. Recently, it has been demonstrated that the multiferroic phase in NiI_2 persists from the bulk to the single-layer limit [6]. Further, it has been shown that a significant enhancement of the helimagnetic order in bulk NiI_2 can be achieved with hydrostatic pressure [13,14] all the way up to 132 K at 5 GPa.

Given that 2D multiferroics would provide disruptive possibilities to electrically control magnetic order, it is interesting to further explore other candidate materials, and analyzing the consequences of changing the halide ion is an obvious strategy to pursue. In this context, $NiBr_2$ is the closest relative of NiI_2 in the dihalide family. $NiBr_2$ crystallizes in a $CdCl_2$ structure (space group $R\bar{3}m$) [15,16] as depicted in Fig. 1. Its structure is formed by edge-sharing $NiBr_6$ octahedra (forming a triangular lattice) that stack along the c axis with weak vdW bonding. The Ni^{2+} (S = 1) Ni ions order antiferromagnetically at $T_{N,1} = 52$ K [15,17,18]. As in NiI_2, this collinear AFM phase consists of ferromagnetic planes coupled antiferromagnetically out of plane. At $T_{N,2} = 23$ K, a second transition occurs to a spin-spiral order [17,18]. Interestingly, akin to NiI_2, $NiBr_2$ also develops a ferroelectric polarization in its helimagnetic low-temperature ground state [19]. Notably, the helimagnetic transition temperature of $NiBr_2$ is considerably lower than that of NiI_2 but hydrostatic pressure could in principle be exploited as a means to enhance it.

Here, we study the effects of hydrostatic pressure on the magnetic properties of bulk $NiBr_2$ using a combination of first-principles calculations and Monte Carlo simulations. Our results indicate that there is a substantial magnetic frustration in $NiBr_2$ (that increases with pressure) arising from the competition between the intralayer ferromagnetic nearest-neighbor interaction ($J^{\parallel 1}$) and the antiferromagnetic third nearest-neighbor interaction ($J^{\parallel 3}$). Such magnetic frustration is at the origin of its helimagnetic ground state whose transition temperature we can accurately reproduce at ambient pressure using Monte Carlo simulations. We find that pressure has a significant effect on the interlayer coupling ($J^{\perp \text{eff}}$), but also on some of the leading intralayer interactions. Using the first-principles-derived magnetic constants, Monte Carlo simulations reveal a threefold increase in the helimagnetic transition temperature of $NiBr_2$ at a modest pressure of 15 GPa.

II. COMPUTATIONAL METHODS

In previous work [14] we analyzed the pressure dependence of the magnetic properties of NiI_2 using a combination of *ab initio* calculations and Monte Carlo simulations. Here, we follow an analog methodology to study the pressure dependence of the magnetic properties in the related material $NiBr_2$ to scrutinize the changes produced by a change in the halide ion. The details on the computational methods employed are explained below.

*Contact author: skbag@asu.edu
†Contact author: onur.erten@asu.edu
‡Contact author: antia.botana@asu.edu

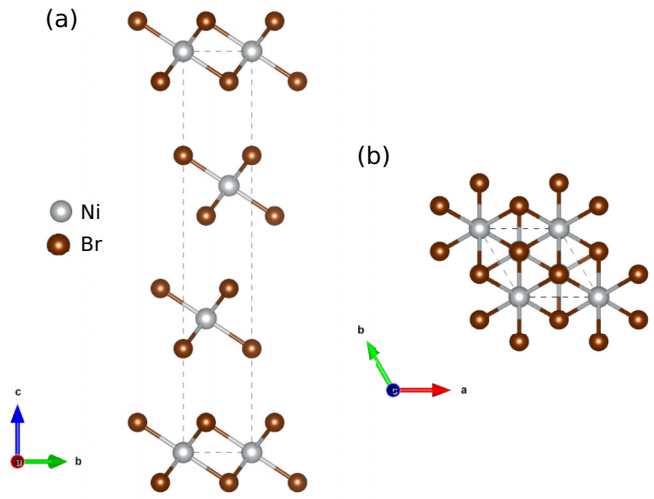

FIG. 1. Crystal structure of bulk $NiBr_2$. Out-of-plane (a) and in-plane (b) views of the $R\bar{3}m$ structure. Ni atoms are represented by gray spheres, while brown spheres represent Br atoms. A black dotted line marks the unit cell boundaries.

First-principles calculations. We performed density functional theory (DFT)-based calculations in $NiBr_2$ using the projector augmented wave (PAW) method [20] as implemented in the VASP code [21,22]. The wave functions were expanded in the plane-wave basis with a kinetic-energy cutoff of 500 eV. We considered the $3p$, $3d$, and $4s$ orbitals ($3p^6 3d^8 4s^2$ configuration) as valence states for the Ni atoms. Meanwhile, for the Br atoms, we considered the $4s$ and $4p$ orbitals ($4s^2 4p^5$ configuration) as valence states.

Hydrostatic pressure was applied in 5 GPa increments (up to 15 GPa), conducting full structural relaxations. The optimization of the bulk unit cells at each pressure involved optimizing atomic positions, cell shape, and cell volume, but focusing exclusively on the rhombohedral phase. The energy and force minimization tolerances were set at 10^{-10} eV and 10^{-3} eV/Å, respectively. The calculations were done using the Perdew-Burke-Ernzerhof (PBE) [23] version of the generalized gradient approximation (GGA) functional, with the inclusion of the DFT-D3 van der Waals correction [24]. Additionally, we incorporated an on-site Coulomb repulsion parameter (U) using the Liechtenstein [25] approach to account for correlation effects in the Ni-d electrons [26]. The U and Hund's coupling J_H values utilized in all the calculations presented in the main text ($U = 3.9$ eV and $J_H = 0.79$ eV) were derived from constrained random phase approximation (cRPA) calculations [27]. For all of the relaxations, we fixed the magnetic configuration to an AFM state comprised of FM planes coupled AFM out of plane. To accommodate the AFM ordering, we employed a $1\times1\times2$ supercell and conducted Brillouin zone (BZ) sampling using a $40\times40\times4$ Monkhorst-Pack k mesh centered on the Γ point. This AFM order aligns with the c component of the magnetic propagation vector ($\sim 3/2$) [3].

Finally, we computed the exchange couplings and anisotropies for $NiBr_2$ using the four-state method, extensively detailed in Refs. [28–32]. This method relies on performing total energy mappings through noncollinear magnetic DFT calculations with spin-orbit coupling (SOC). Each magnetic interaction parameter is associated with the energies of four distinct magnetic configurations, wherein the directions of the magnetic moments are constrained, and large supercells are employed to prevent coupling between distant neighbors. Using this methodology, intralayer (interlayer) magnetic constants were calculated for each pressure.

Monte Carlo simulations. We employed the Matjes [33] code to conduct Monte Carlo simulations in $NiBr_2$ to further investigate its magnetic response with pressure. Around $\sim 10^6$ thermalization steps were executed at each temperature, followed by $\sim 10^4$ Monte Carlo steps for statistical averaging. The simulations utilized a standard metropolis algorithm on supercells with dimensions $L\times L\times 4$ and periodic boundary conditions. To determine the supercell size L, we adopted the criterion $L \simeq nL_{\text{m.u.c.}}$, where n is an integer, and $L_{\text{m.u.c.}}$ represents the minimum lateral size of the magnetic unit cell. The length of the magnetic unit cell $L_{\text{m.u.c.}}$ was estimated as $L_{\text{m.u.c.}} \sim 1/q^{\parallel}$, where $q^{\parallel}$ denotes the magnitude of the in-plane component of the magnetic propagation vector derived as $q^{\parallel} = \frac{1}{2\pi}\arccos\left[(1+\sqrt{1-2(J^{\parallel 1}/J^{\parallel 3})})/4\right]$ [34,35].

III. RESULTS

We start by introducing the microscopic model that we will follow to obtain the relevant magnetic interactions for $NiBr_2$, given by the following Heisenberg Hamiltonian between localized spins $\mathbf{S}_i$ that we split into intra and interlayer contributions expressed as $H^{\parallel}$ and $H^{\perp}$, respectively,

$$H^{\parallel} = \frac{1}{2}\sum_{i\neq j}\mathbf{S}_i\cdot\mathbf{J}^{\parallel}_{ij}\cdot\mathbf{S}_j + \sum_i \mathbf{S}_i\cdot\mathbf{A}_i\cdot\mathbf{S}_i, \tag{1}$$

$$H^{\perp} = \frac{1}{2}\sum_{i,j} J^{\perp}_{ij}\mathbf{S}_i\cdot\mathbf{S}_j. \tag{2}$$

Here, the indices i and j refer to the Ni atom sites. In Eq. (1), $\mathbf{A}_i$ denotes the on-site or single-ion anisotropy (SIA) and $\mathbf{J}_{ij}$ represents the intralayer exchange coupling interaction tensor. The latter can be decomposed into two contributions for $NiBr_2$: an isotropic coupling term, and an anisotropic symmetric term (the antisymmetric term which corresponds to the Dzyaloshinskii-Moriya interaction vanishes in $NiBr_2$ due to the presence of inversion symmetry). $J^{\perp}_{ij}$ in Eq. (2) represents the isotropic interlayer exchange constant between spins $\mathbf{S}_{i,j}$. We consider up to third nearest-neighbor isotropic exchanges both in-plane and out-of-plane. The full tensor is only taken into account for the in-plane nearest-neighbor exchange interaction. The factors of $1/2$ are used to account for double counting. The sign conventions used here are as follows: a positive (negative) isotropic exchange interaction favors an antiparallel (parallel) alignment of spins and a positive (negative) scalar single-ion parameter indicates an easy-plane (easy-axis) anisotropy.

Before moving into the evolution of the relevant magnetic parameters, we start by describing the evolution of the structural properties of $NiBr_2$ under pressure. Figure 2 displays the relaxed lattice parameters of $NiBr_2$ as a function of pressure obtained from our first-principles calculations using the computational parameters described in Sec. II. Upon applying hydrostatic pressure, both the in-plane (see Fig. 2(a)) and

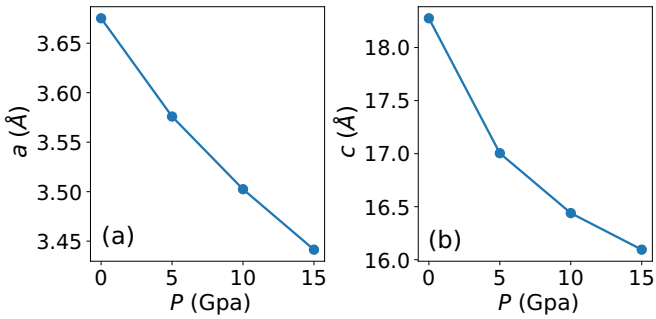

FIG. 2. First-principles derived (a) in-plane and (b) out-of-plane relaxed lattice parameters as a function of pressure (P) for bulk $NiBr_2$.

out-of-plane (see Fig. 2(b)) lattice parameters decrease monotonically, with a much larger decrease in the out-of-plane lattice parameter, as expected for a van der Waals material. Specifically, a decreases from 3.67 Å at ambient pressure to 3.44 Å at 15 GPa while c decreases from 18.27 Å to 16.09 Å at 15 GPa.

The basic evolution of the electronic structure is shown in Appendix A. Up to the highest pressures studied here, $NiBr_2$ remains insulating within our GGA + U calculations (the gap can only be closed at ∼80 GPa). The derived magnetic moment for the Ni atoms is $\sim 1.54\,\mu_B$ at all pressures, consistent with high-spin Ni^{2+} but with a slightly reduced value with respect to the nominal one due to hybridization with the Br ligands (with moments $\sim 0.17\,\mu_B$ at all pressures). Our first-principles derived magnetic moments are in good agreement with the ordered experimental Ni moment values obtained at ambient pressure $\sim 1.5\,\mu_B$ [3,36].

After establishing the basics of the evolution of the structure and electronic structure in the AFM collinear phase, next we move on to the calculations of the magnetic coupling constants for $NiBr_2$ using the four-state method (we followed the implementation used for other dihalides as described in Refs. [4,14,37]). Table I presents the computed intralayer and interlayer magnetic parameters introduced in Eqs. (1) and (2), as well as relevant ratios between magnetic couplings for pressures up to 15 GPa. Figure 3(a) shows the evolution of these relevant magnetic exchange ratios as a function of pressure while Fig. 3(b) shows the paths for the dominant exchange interactions. At ambient pressure, the largest exchange interaction in $NiBr_2$ is the ferromagnetic (FM) intralayer first nearest-neighbor exchange ($J^{\parallel 1} \sim -3.2$ meV). The second nearest-neighbor exchange is vanishingly small and FM, while the third nearest-neighbor intralayer exchange is AFM and sizable ($J^{\parallel 3} \sim 1.6$ meV). In comparison to NiI_2 [14], the FM nearest-neighbor exchange is smaller (−3.2 meV for $NiBr_2$ vs −4.5 meV for NiI_2) but it is the AFM third nearest-neighbor exchange that gets further reduced by the change in the ligand p states (1.6 meV for $NiBr_2$ vs 3.7 meV for NiI_2). Note that derivation of a large J for third (vs second) nearest-neighbors is consistent with previous results obtained for dihalide monolayers in Ref. [27]: for second nearest-neighbors, only the t_{2g}-e_g hopping is relevant at d^8 filling, leading to a weak FM interaction, while for third nearest neighbors, there are large e_g-e_g hoppings that arise from

TABLE I. Calculated $NiBr_2$ isotropic intralayer exchange interactions (top panel), interlayer isotropic interactions (bottom panel), SIA (A), and first-nearest neighbor in-plane two-site anisotropy (TSA) constants (middle panel) in a cartesian x, y, z reference system where x was chosen to be parallel to the Ni-Ni bonding vector for different pressures (P). $J^{\perp\text{eff}}$ represents the effective interlayer exchange and is obtained as $J^{\perp 1} + J^{\perp 2} + 2J^{\perp 3}$, where the coefficient in the last term arises because there are twice as many out-of-plane third nearest-neighbors as first and second nearest-neighbors. Pressure is in units of GPa, and exchange constants are given in units of meV.

Isotropic intralayer exchanges

P	$J^{\parallel 1}$	$J^{\parallel 2}$	$J^{\parallel 3}$	$J^{\parallel 3}/J^{\parallel 1}$
0	−3.19	−0.05	1.56	−0.49
5	−3.71	−0.06	2.25	−0.61
10	−4.24	−0.14	2.92	−0.69
15	−4.68	−0.17	3.74	−0.8

SIA and intralayer TSA

P	A	$J^{S\parallel 1}_{xx}$	$J^{S\parallel 1}_{yy}$	$J^{S\parallel 1}_{zz}$	$J^{S\parallel 1}_{yz}$	$J^{S\parallel 1}_{yz}/J^{\parallel 1}$
0	0.0	−0.04	0.04	0.0	−0.06	0.019
5	0.0	−0.05	0.04	0.0	−0.07	0.018
10	0.0	−0.05	0.05	0.0	−0.07	0.018
15	0.03	−0.2	0.13	0.07	−0.08	0.017

Isotropic interlayer exchanges

P	$J^{\perp 1}$	$J^{\perp 2}$	$J^{\perp 3}$	$J^{\perp\text{eff}}$	$J^{\perp 2}/J^{\parallel 1}$
0	0.01	0.62	0.17	0.96	−0.19
5	0.01	1.7	0.42	2.54	−0.46
10	0.02	2.84	0.67	4.19	−0.67
15	0.12	4.02	0.9	5.94	−0.85

hopping paths that are ligand assisted. Importantly, the competition between intralayer FM $J^{\parallel 1}$ and AFM $J^{\parallel 3}$ (measured by the ratio $J^{\parallel 3}/J^{\parallel 1} = -0.5$) gives rise to magnetic frustration which favors the realization of the noncollinear magnetic ground state of $NiBr_2$ [38] (in a similar fashion to NiI_2 [14] but with a smaller $J^{\parallel 3}/J^{\parallel 1}$ ratio being obtained [−0.5 for $NiBr_2$ vs −0.8 for NiI_2]). Another critical parameter in the context of magnetic exchanges is the ratio $J^{S\parallel 1}_{yz}/J^{\parallel 1}$ which gauges the canting of the two-site anisotropy axes from the direction perpendicular to the layers [4]. This ratio is estimated to be very small in $NiBr_2$ $J^{S\parallel 1}_{yz}/J^{\parallel 1} = 0.019$, in contrast to NiI_2 where a ratio one order of magnitude larger is derived $J^{S\parallel 1}_{yz}/J^{\parallel 1} = 0.19$. Moving to the interlayer exchange interactions, they are all AFM in nature with the second nearest-neighbor $J^{\perp 2}$ being the dominant one ∼0.6 meV, similar to NiI_2 but once again with a considerably reduced value (0.6 meV vs 1.5 meV). If we look at the ratio between the dominant intra vs interlayer interactions in $NiBr_2$ $J^{\perp 2}/J^{\parallel 1} \sim -0.2$ at ambient pressure, in contrast to the larger $J^{\perp 2}/J^{\parallel 1}$ for NiI_2 of −0.32.

As in NiI_2, the signs of the dominant intra and interlayer interactions do not change with pressure but the magnitude of the isotropic magnetic constants increases considerably. For the first nearest-neighbor isotropic exchange $J^{\parallel 1}_{15\text{GPa}} = 1.5\,J^{\parallel 1}_{0\text{GPa}}$, for the third nearest-neighbor isotropic exchange $J^{\parallel 3}_{15\text{GPa}} = 2.4\,J^{\parallel 3}_{0\text{GPa}}$, while the second nearest-neighbor $J^{\parallel 2}$ remains vanishingly small at all pressures. The

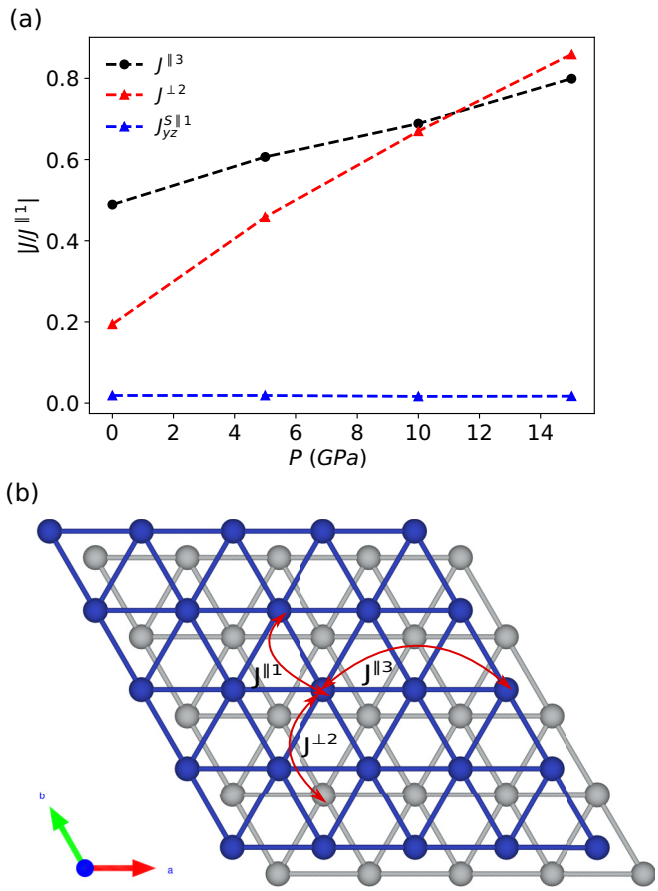

FIG. 3. (a) Pressure evolution of the three relevant ratios of exchange couplings $J^{\parallel 3}/J^{\parallel 1}$, $J^{\perp 2}/J^{\parallel 1}$, $J_{yz}^{S\parallel 1}/J^{\parallel 1}$ for bulk $NiBr_2$. (b) The paths for the dominant exchange interactions $J^{\parallel 1}$, $J^{\parallel 3}$, and $J^{\perp 2}$ are shown over the triangular arrangement of Ni atoms in $NiBr_2$ (with gray spheres corresponding to Ni atoms in the bottom layer and blue spheres to those in the top layer).

pressure-dependent response of the dominant intralayer isotropic exchanges can be understood by looking at the relevant hopping amplitudes, as we showed before for NiI_2 [14]. For $J^{\parallel 1}$ there are two primary contributions, one being FM (mainly arising from the hopping process between t_{2g} and e_g states via the ligand p states) and the other AFM (mainly arising from direct d-d overlap between Ni t_{2g}-like states). With increasing pressure, the FM contribution increases at a faster rate resulting in an overall increase of $J^{\parallel 1}$ even though the competition due to the AFM hoppings still persists. In contrast, $J^{\parallel 3}$ exhibits solely AFM contributions originating from e_g-e_g hoppings, as mentioned above, without FM contributions. In this manner, the $J^{\parallel 3}/J^{\parallel 1}$ ratio undergoes a sizable increase with pressure from -0.5 at ambient pressure to -0.8 at 15 GPa [see Fig. 3(a)]. In NiI_2 this change is significantly larger (from -0.81 to -2.16) due once again to the broader I-p states. The single-ion anisotropy is negligible at all pressures, and the intralayer anisotropic exchanges ($J_{yz}^{S\parallel 1}$) exhibit minimal changes with pressure as well. The ratio $J_{yz}^{S\parallel 1}/J^{\parallel 1}$ remains nearly constant (and small) up to 15 GPa, as depicted in Fig. 3(a).

Regarding the interlayer exchanges, the signs of the dominant interlayer isotropic exchange interactions persist as well (as they do in NiI_2 [14]): both $J^{\perp 2}$ and $J^{\perp 3}$ remain antiferromagnetic in the pressure range studied here, even though they increase sizably with pressure ($J^{\perp 1}$ remains small in comparison). This substantial increase is particularly noticeable for the dominant second nearest-neighbor interlayer exchange $J_{15\mathrm{GPa}}^{\perp 2} = 6.5\, J_{0\mathrm{GPa}}^{\perp 2}$. Such a large increase can be attributed to the significant decrease in the c lattice parameter with pressure described above, as expected in a vdW material. Importantly, $J^{\perp 2}$ at 15 GPa becomes the second largest interaction overall, closely competing in value with $J^{\parallel 1}$ [see Fig. 3(a)]. In NiI_2 the situation is, once more, quantitatively different: the sevenfold increase in $J^{\perp 2}$ causes it to quickly surpass the dominant in-plane exchange already at 10 GPa.

The magnetic constants derived from the four-state method for $NiBr_2$ were subsequently used in Monte Carlo simulations. At low temperatures, we confirm that the derived magnetic ground state is a spin spiral (this is consistent with previous DFT-based studies that reported a spin-spiral ground state in monolayer $NiBr_2$ [39–41], see the corresponding magnetic texture and structure factor in Appendix B). From our pressure-dependent specific heat calculations we can clearly observe a magnetic transition at a temperature T_N, indicated by the dashed vertical line in Fig. 4(a), that increases

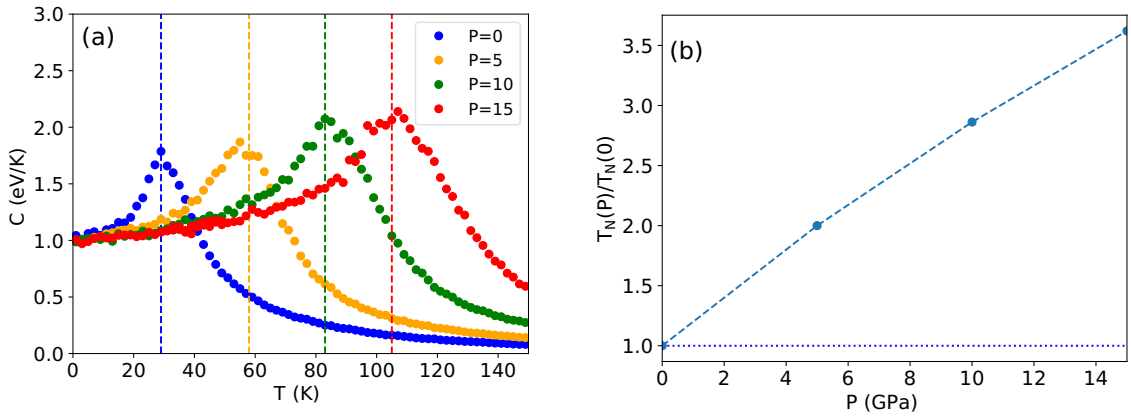

FIG. 4. (a) Specific heat C of bulk $NiBr_2$ as a function of temperature T for various pressures P = 0, 5, 10, and 15 GPa obtained from Monte Carlo simulations. The dashed lines indicate the critical temperature T_N at each pressure: 29, 58, 83, and 105 K for 0, 5, 10, and 15 GPa, respectively. (b) Ambient-pressure-normalized critical temperature values for bulk $NiBr_2$ as a function of pressure P.

monotonically with pressure. Although some double-peak structure can be observed (that was also obtained in similar calculations for NiI_2 [14]), we focus here on a qualitative understanding of the trends in the magnetic response with pressure, rather than pursuing a quantitative description of the two magnetic transitions. Figure 4(b) clearly shows the monotonic increase of T_N as a function of pressure, with the data points being normalized relative to the value calculated at ambient pressure [T_N(0 GPa)=29 K, very close to the experimentally derived value of ∼23 K]. Notably, our calculated T_N undergoes a threefold increase between 0 and 15 GPa (rising from 29 to 105 K). Such an increase is almost identical to the one achieved for NiI_2 at the same pressure, in spite of the quantitative differences in magnetic parameters described in detail above, obtained as a consequence of the change in halide ion.

Importantly, the increase in the $J^{\parallel 3}/J^{\parallel 1}$ ratio with pressure we have found in $NiBr_2$ has important implications for the helimagnetic propagation vector and likely for the related spin-induced ferroelectric polarization, as we also showed for NiI_2. As mentioned in Sec. II, the in-plane component of the magnetic propagation vector can be determined as $q^{\parallel} = 2\arccos[(1+\sqrt{1-2(J^{\parallel 1}/J^{\parallel 3})})/4]$, the related spin-induced ferroelectric order can be estimated as $P \propto \sin(q)$ by the generalized Katsura-Nagaosa-Balatsky model [6,12,42]. The observed increase in $J^{\parallel 3}/J^{\parallel 1}$ with pressure favors a larger q (shorter in-plane spiral pitch) which, potentially, can then give rise to a larger spin-induced polarization (see Appendix C for further details).

Overall, the magnetic ground state of $NiBr_2$ (and its evolution under pressure) is qualitatively similar to that of NiI_2 [13,14]. Both compounds have the same dominant exchange couplings ($J^{\parallel 1}$, $J^{\parallel 3}$, and $J^{\perp 2}$) and exhibit spin spiral order governed by the magnetic frustration arising from the competition between $J^{\parallel 1}$ and $J^{\parallel 3}$. Some quantitative differences are obtained in the absolute values of the dominant exchanges (dictated by the larger spatial extent of I-p vs Br-p states) but, in spite of those differences, the estimated change in magnetic transition temperature with pressure ends up being almost identical in the two materials (threefold at 15 GPa). One important distinction is that in NiI_2 the magnetic transition temperature saturates already at 10 GPa (in both theory and experiments [13,14]) but in $NiBr_2$, saturation is not yet achieved at 15 GPa in our calculations. This, together with the higher stability of $NiBr_2$, make this system a promising platform to study in the context of helimagnetism (and multiferroicity) in 2D vdW materials.

IV. SUMMARY

To summarize, we employed first-principles calculations combined with Monte Carlo simulations to investigate the impact of hydrostatic pressure on the magnetic properties of bulk $NiBr_2$. Using the four-state method, we computed the intralayer and interlayer exchange parameters (up to third nearest neighbors) of the low energy effective spin model for bulk $NiBr_2$. The low-temperature magnetic ordering corresponds to a spin spiral that is governed by the magnetic frustration between the two dominant in-plane exchange terms ($J^{\parallel 1}$ and $J^{\parallel 3}$), exhibiting different signs (ferro and antiferromagnetic, respectively). The interlayer exchanges were identified as antiferromagnetic, with $J^{\perp 2}$ being the dominant interaction. With increasing pressure, all the dominant exchange couplings ($J^{\parallel 1}$, $J^{\parallel 3}$, and $J^{\perp 2}$) increase monotonically, and consequently, the (heli)-magnetic ordering temperature increases. These results suggest that hydrostatic pressure holds promise as a means to enhance the magnetic response of $NiBr_2$. Even though we do not analyze here the corresponding induced electric polarization, we anticipate that pressure could also potentially enhance the concomitant multiferroic response of $NiBr_2$.

ACKNOWLEDGMENT

S.B., J.K., O.E., and A.B. acknowledge support from NSF Grant No. DMR-2206987 and the ASU Research Computing Center for high-performance computing resources.

APPENDIX A: BAND STRUCTURE EVOLUTION WITH PRESSURE FOR $NiBr_2$

Figure 5 shows the evolution of the band structure along high-symmetry directions for $NiBr_2$ in the collinear and AFM state (consisting of ferromagnetic planes coupled antiferromagnetically out-of-plane) under hydrostatic pressure. The band gap can only be closed at ∼80 GPa.

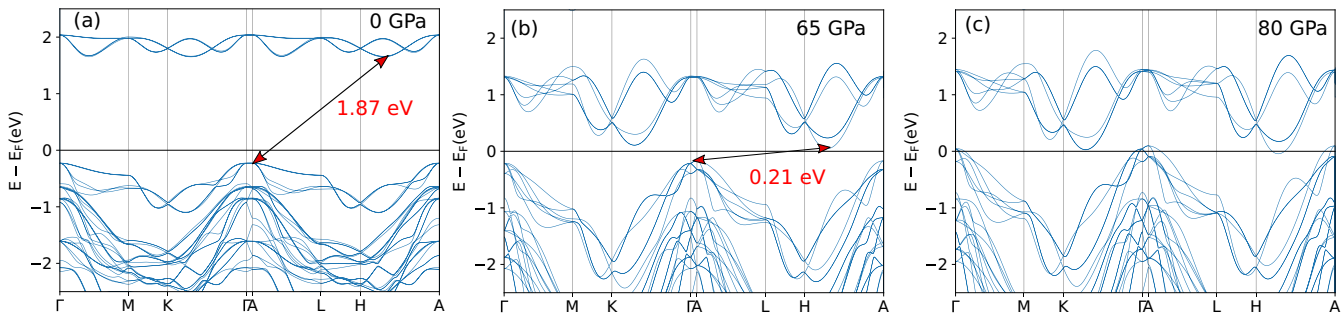

FIG. 5. GGA-PBE+D3+U band structure plots for bulk $NiBr_2$ (calculated with AFM order and $U = 3.9$ eV) at ambient pressure (a), 65 GPa (b), and 80 GPa (c) where the energy band gaps are indicated in the insulating 0 and 65 GPa cases. Reciprocal space coordinates: Γ = (0, 0, 0), M = (1/2, 0, 0), K = (1/3, 1/3, 0), A = (0, 0, 1/2), L = (1/2, 0, 1/2), and H = (1/3, 1/3, 1/2).

TABLE II. Indirect band gap E_{gap} of bulk $NiBr_2$ as a function of pressure. Here, a zero band gap value corresponds to a metallic state.

P (GPa)	E_{gap}
0	1.8737
5	1.7282
10	1.5999
15	1.4630
40	0.8075
65	0.2137
80	0.0

TABLE III. Ratio of the leading intralayer exchanges $J^{\parallel 1}/J^{\parallel 3}$, in-plane component of the magnetic propagation vector magnitude $q^{\parallel}$, and magnetic unit cell length $L_{\text{m.u.c.}}$ for bulk $NiBr_2$ at pressures (P) up to 15 GPa.

P (GPa)	$J^{\parallel 1}/J^{\parallel 3}$	$q^{\parallel}$	$L_{\text{m.u.c.}}$
0	−2.05	0.098	10.14
5	−1.65	0.110	9.05
10	−1.45	0.116	8.59
15	−1.25	0.122	8.16

Table II contains the corresponding indirect band gap E_{gap} of bulk $NiBr_2$ as a function of pressure.

APPENDIX B: MAGNETIZATION TEXTURES OF MONOLAYER $NiBr_2$

Figure 6(a) shows the magnetization texture of monolayer $NiBr_2$ (10×10 supercell) at P = 0 and T = 1 K, which exhibits a spin-spiral structure along the x direction. The spin-spiral structure along the x direction is confirmed by the spin structure factor data shown in Fig. 6(b). The spin structure factor for momentum $\mathbf{q}$ is defined as

$$S(\mathbf{q}) = \frac{1}{N}\sum_{\alpha=x,y,z}\left\langle\left|\sum_i s_{i\alpha}e^{-i\mathbf{q}\cdot\mathbf{r}_i}\right|^2\right\rangle, \tag{B1}$$

where $N = L^2$ is the total number of spins and $s_{i\alpha}$ denotes the α component of the spin at site i with position of site $\mathbf{r}_i$. This calculated spin structure factor is nonzero at two $\mathbf{q}$ points in momentum space.

APPENDIX C: MAGNETIC PROPAGATION VECTOR

Table III contains the important exchange interaction ratio between $J^{\parallel 1}$ and $J^{\parallel 3}$ for bulk $NiBr_2$ for pressures up to 15 GPa. As mentioned in the main text, these exchange interactions are calculated using the four-state method. From this exchange interaction ratio, we calculate the in-plane component of the magnetic propagation vector $q^{\parallel} = \frac{1}{2\pi}\arccos\left[(1+\sqrt{1-2(J^{\parallel 1}/J^{\parallel 3})})/4\right]$ which gives the magnetic unit cell size $L_{\text{m.u.c.}} \sim 1/q^{\parallel}$ [34,35]. With increasing pressure, the ratio $|J^{\parallel 1}/J^{\parallel 3}|$ decreases, resulting in an increasing $q^{\parallel}$ with pressure. Such an increase in $q^{\parallel}$ with pressure corresponds to a decreasing $L_{\text{m.u.c.}}$, which means that the magnetic unit cells gets smaller with increasing pressure.

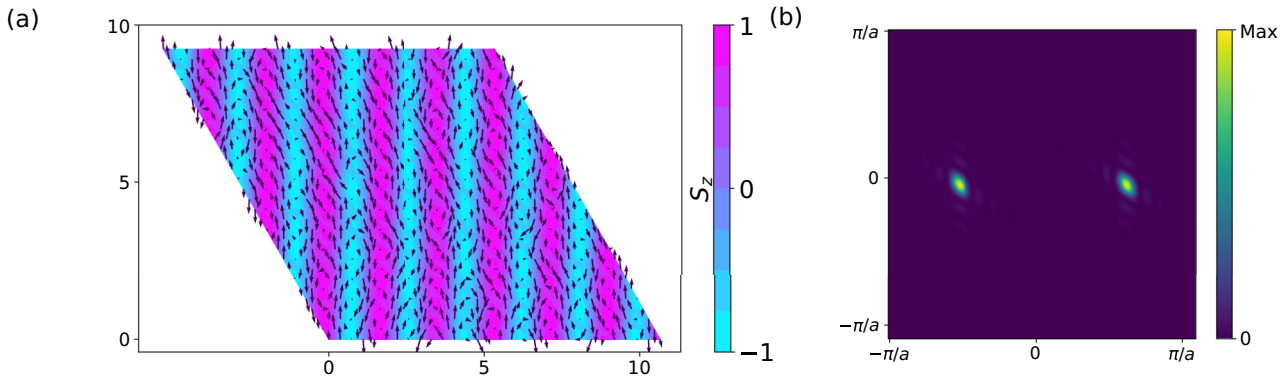

FIG. 6. (a) Magnetization texture: black arrows represent the in-plane s_x, s_y spin components; the colormap indicates the out-of-plane s_z spin component and (b) spin structure factor of monolayer $NiBr_2$ at ambient pressure at 1 K.

[1] M. Blei, J. L. Lado, Q. Song, D. Dey, O. Erten, V. Pardo, R. Comin, S. Tongay, and A. S. Botana, Synthesis, engineering, and theory of 2D van der Waals magnets, Appl. Phys. Rev. **8**, 021301 (2021).

[2] M. Gibertini, M. Koperski, A. F. Morpurgo, and K. S. Novoselov, Magnetic 2D materials and heterostructures, Nat. Nanotechnol. **14**, 408 (2019).

[3] M. A. McGuire, Crystal and magnetic structures in layered, transition metal dihalides and trihalides, Crystals **7**, 121 (2017).

[4] D. Amoroso, P. Barone, and S. Picozzi, Spontaneous skyrmionic lattice from anisotropic symmetric exchange in a Ni-halide monolayer, Nat. Commun. **11**, 5784 (2020).

[5] H. Ju, Y. Lee, K.-T. Kim, I. H. Choi, C. J. Roh, S. Son, P. Park, J. H. Kim, T. S. Jung, J. H. Kim, K. H. Kim, J.-G. Park, and J. S. Lee, Possible persistence of multiferroic order down to bilayer limit of van der waals material NiI_2, Nano Lett. **21**, 5126 (2021).

[6] Q. Song, C. A. Occhialini, E. Ergeçen, B. Ilyas, D. Amoroso, P. Barone, J. Kapeghian, K. Watanabe, T. Taniguchi, A. S. Botana, S. Picozzi, N. Gedik, and R. Comin, Evidence for a single-layer van der Waals multiferroic, Nature (London) **602**, 601 (2022).

[7] A. O. Fumega and J. L. Lado, Microscopic origin of multiferroic order in monolayer NiI_2, 2D Mater. **9**, 025010 (2022).

[8] D. Lebedev, J. T. Gish, E. S. Garvey, T. K. Stanev, J. Choi, L. Georgopoulos, T. W. Song, H. Y. Park, K. Watanabe, T. Taniguchi, N. P. Stern, V. K. Sangwan, and M. C. Hersam, Electrical interrogation of thickness-dependent multiferroic phase transitions in the 2D antiferromagnetic semiconductor NiI_2, Adv. Funct. Mater. **33**, 2212568 (2023).

[9] J. Das, M. Akram, and O. Erten, Revival of antibiskyrmionic magnetic phases in bilayer NiI_2, Phys. Rev. B **109**, 104428 (2024).

[10] D. Billerey, C. Terrier, N. Ciret, and J. Kleinclauss, Neutron diffraction study and specific heat of antiferromagnetic NiI_2, Phys. Lett. A **61**, 138 (1977).

[11] D. Billerey, C. Terrier, R. Mainard, and A. Pointon, Magnetic phase transition in anhydrous NiI_2, Phys. Lett. A **77**, 59 (1980).

[12] T. Kurumaji, S. Seki, S. Ishiwata, H. Murakawa, Y. Kaneko, and Y. Tokura, Magnetoelectric responses induced by domain rearrangement and spin structural change in triangular-lattice helimagnets NiI_2 and CoI_2, Phys. Rev. B **87**, 014429 (2013).

[13] C. A. Occhialini, L. G. P. Martins, Q. Song, J. S. Smith, J. Kapeghian, D. Amoroso, J. J. Sanchez, P. Barone, B. Dupé, M. J. Verstraete, J. Kong, A. S. Botana, and R. Comin, Signatures of pressure-enhanced helimagnetic order in van der Waals multiferroic NiI_2, arXiv:2306.11720.

[14] J. Kapeghian, D. Amoroso, C. A. Occhialini, L. G. P. Martins, Q. Song, J. S. Smith, J. J. Sanchez, J. Kong, R. Comin, P. Barone, B. Dupé, M. J. Verstraete, and A. S. Botana, Effects of pressure on the electronic and magnetic properties of bulk NiI_2, Phys. Rev. B **109**, 014403 (2024).

[15] P. Day, A. Dinsdale, E. R. Krausz, and D. J. Robbins, Optical and neutron diffraction study of the magnetic phase diagram of $NiBr_2$, J. Phys. C **9**, 2481 (1976).

[16] J. Nasser, J. Kiat, and R. Gabilly, X-ray investigation of magnetostriction in $NiBr_2$, Solid State Commun. **82**, 49 (1992).

[17] P. Day and K. R. A. Ziebeck, Incommensurate spin structure in the low-temperature magnetic phase of $NiBr_2$, J. Phys. C **13**, L523 (1980).

[18] A. Adam, D. Billerey, C. Terrier, R. Mainard, L. Regnault, J. Rossat-Mignod, and P. Mériel, Neutron diffraction study of the commensurate and incommensurate magnetic structures of $NiBr_2$, Solid State Commun. **35**, 1 (1980).

[19] Y. Tokunaga, D. Okuyama, T. Kurumaji, T. Arima, H. Nakao, Y. Murakami, Y. Taguchi, and Y. Tokura, Multiferroicity in $NiBr_2$ with long-wavelength cycloidal spin structure on a triangular lattice, Phys. Rev. B **84**, 060406(R) (2011).

[20] G. Kresse and D. Joubert, From ultrasoft pseudopotentials to the projector augmented-wave method, Phys. Rev. B **59**, 1758 (1999).

[21] G. Kresse and J. Furthmüller, Efficient iterative schemes for *ab initio* total-energy calculations using a plane-wave basis set, Phys. Rev. B **54**, 11169 (1996).

[22] G. Kresse and J. Furthmüller, Efficiency of ab-initio total energy calculations for metals and semiconductors using a plane-wave basis set, Comput. Mater. Sci. **6**, 15 (1996).

[23] J. P. Perdew, K. Burke, and M. Ernzerhof, Generalized gradient approximation made simple, Phys. Rev. Lett. **77**, 3865 (1996).

[24] S. Grimme, J. Antony, S. Ehrlich, and H. Krieg, A consistent and accurate *ab initio* parametrization of density functional dispersion correction (DFT-D) for the 94 elements H-Pu, J. Chem. Phys. **132**, 154104 (2010).

[25] A. I. Liechtenstein, V. I. Anisimov, and J. Zaanen, Density-functional theory and strong interactions: Orbital ordering in Mott-Hubbard insulators, Phys. Rev. B **52**, R5467 (1995).

[26] A. Rohrbach, J. Hafner, and G. Kresse, Electronic correlation effects in transition-metal sulfides, J. Phys.: Condens. Matter **15**, 979 (2003).

[27] K. Riedl, D. Amoroso, S. Backes, A. Razpopov, T. P. T. Nguyen, K. Yamauchi, P. Barone, S. M. Winter, S. Picozzi, and R. Valentí, Microscopic origin of magnetism in monolayer 3*d* transition metal dihalides, Phys. Rev. B **106**, 035156 (2022).

[28] H. Xiang, C. Lee, H.-J. Koo, X. Gong, and M.-H. Whangbo, Magnetic properties and energy-mapping analysis, Dalton Trans. **42**, 823 (2013).

[29] H. J. Xiang, E. J. Kan, S.-H. Wei, M.-H. Whangbo, and X. G. Gong, Predicting the spin-lattice order of frustrated systems from first principles, Phys. Rev. B **84**, 224429 (2011).

[30] D. Šabani, C. Bacaksiz, and M. V. Milošević, *Ab initio* methodology for magnetic exchange parameters: Generic four-state energy mapping onto a Heisenberg spin Hamiltonian, Phys. Rev. B **102**, 014457 (2020).

[31] C. Xu, J. Feng, H. Xiang, and L. Bellaiche, Interplay between Kitaev interaction and single ion anisotropy in ferromagnetic CrI_3 and $CrGeTe_3$ monolayers, npj Comput. Mater. **4**, 57 (2018).

[32] C. Xu, J. Feng, S. Prokhorenko, Y. Nahas, H. Xiang, and L. Bellaiche, Topological spin texture in Janus monolayers of the chromium trihalides $Cr(I, X)_3$, Phys. Rev. B **101**, 060404(R) (2020).

[33] B. D. *et al.* github.com/bertdupe/matjes

[34] S. Hayami, S.-Z. Lin, and C. D. Batista, Bubble and skyrmion crystals in frustrated magnets with easy-axis anisotropy, Phys. Rev. B **93**, 184413 (2016).

[35] C. D. Batista, S.-Z. Lin, S. Hayami, and Y. Kamiya, Frustration and chiral orderings in correlated electron systems, Rep. Prog. Phys. **79**, 084504 (2016).

[36] D. Bikaljevic, C. González-Orellana, M. Pena-Díaz, D. Steiner, J. Dreiser, P. Gargiani, M. Foerster, M. A. Nino, L. Aballe, S. Ruiz-Gomez *et al.*, Noncollinear magnetic order in two-

dimensional $NiBr_2$ films grown on Au (111), ACS Nano **15**, 14985 (2021).

[37] T. Gorkan, J. Das, J. Kapeghian, M. Akram, J. V. Barth, S. Tongay, E. Akturk, O. Erten, and A. S. Botana, Skyrmion formation in Ni-based Janus dihalide monolayers: Interplay between magnetic frustration and Dzyaloshinskii-Moriya interaction, Phys. Rev. Mater. **7**, 054006 (2023).

[38] E. Rastelli, A. Tassi, and L. Reatto, Non-simple magnetic order for simple hamiltonians, Physica B+C **97**, 1 (1979).

[39] D. Amoroso, P. Barone, and S. Picozzi, Interplay between single-ion and two-ion anisotropies in frustrated 2D semiconductors and tuning of magnetic structures topology, Nanomaterials **11**, 1873 (2021).

[40] J. Sødequist and T. Olsen, Type II multiferroic order in two-dimensional transition metal halides from first principles spin-spiral calculations, 2D Mater. **10**, 035016 (2023).

[41] D.-W. Wu, Y.-B. Yuan, S. Liu, M.-Q. Long, and Y.-P. Wang, First-principles study of spin-orbital coupling induced ferroelectricity in $NiBr_2$, Phys. Rev. B **108**, 054429 (2023).

[42] H. J. Xiang, E. J. Kan, Y. Zhang, M.-H. Whangbo, and X. G. Gong, General theory for the ferroelectric polarization induced by spin-spiral order, Phys. Rev. Lett. **107**, 157202 (2011).